Analytical behavior of concrete-encased CFST columns under cyclic lateral loading

Wei-Wu Qian [a], Wei Li [a,*], Lin-Hai Han [a], Xiao-Ling Zhao [b,1]

[a] Department of Civil Engineering, Tsinghua University, Beijing 100084, PR China
[b] Department of Civil Engineering, Monash University, Clayton, VIC 3800, Australia

ARTICLE INFO

ABSTRACT

The analytical behavior of concrete-encased CFST (concrete-filled steel tube) columns under cyclic lateral loading is reported in this paper. A finite element analysis (FEA) model is developed to investigate the cyclic behavior of such composite column. Comparisons are made between measured and predicted results on failure modes, load versus displacement relationships and ultimate strength. It is found that the proposed FEA model can reproduce the experimental results with good accuracy. The full-range load–displacement relationships, the contact stress between steel tube and concrete and the axial load distribution among different components are analyzed using the verified FEA model. The cyclic behavior of concrete-encased CFST is compared with that of conventional CFST and reinforced concrete (RC) columns. The parametric analysis is conducted to investigate influences of various parameters on the moment–curvature $(M - \phi)$ envelope curves. The parameters include the material strength, the steel ratio of inner CFST, the longitudinal reinforcement ratio, the stirrup characteristic value, the tube diameter to cross-sectional width ratio (D/B) and the axial load level. Finally, a simplified hysteretic model for the $M - \phi$ relationship of concrete-encased CFST column is proposed.

© 2016 Elsevier Ltd. All rights reserved.

1. Introduction

Concrete-encased concrete-filled steel tubular (concrete-encased CFST) columns consist of inner concrete-filled steel tube (CFST) and outer reinforced concrete (RC) [1]. They have been used in high-rise buildings and bridges. Fig. 1(a) and (b) shows a concrete-encased CFST column under construction and the schematic view of its cross section, respectively. When the column is used in high-rise building, it may be subjected to constant axial load and cyclic lateral loading, as shown in Fig. 1(c).

Extensive studies have been conducted to analyze the static behavior of concrete-encased CFST column under axial compression, pure bending, as well as combined compression and bending, which contribute to reveal the performance of these columns [1,2,3]. However, the research on the seismic performance of concrete-encased CFST column was rather limited, and was mainly focused on experimental investigations of composite columns under cyclic lateral loading. Han et al. [4] conducted tests of concrete-encased CFST beam-columns under constant axial load and cyclically increasing lateral loading. It was found that concrete-encased CFST columns exhibited favorable energy dissipation and ductility even when subjected to high axial load levels.

Ji et al. [5] carried out experiments of concrete-encased CFST columns with different axial load levels and volumetric ratios of stirrups. The results showed that concrete-encased CFST columns had high strength and good ductility. Li et al. [6] conducted tests on high-strength concrete-encased CFST columns under cyclic lateral loading. The load distributions between the inner CFST and outer RC components were analyzed according to experimental results. However, there is a lack of numerical model which could reproduce the behavior of concrete-encased CFST columns under cyclic loading with favorable accuracy. The analytical model is also useful to study the full-range response of concrete-encased CFST columns under cyclic lateral loading.

This paper presents an investigation on the analytical behavior of concrete-encased CFST columns under cyclic lateral loading. The main objectives of this research are threefold. Firstly, to develop a nonlinear 3-D finite element analysis (FEA) model on composite columns under cyclic loading with consideration of the cumulative damage of concrete as well as the interaction between concrete and steel. Secondly, to present analytical results of concrete-encased CFST columns under cyclic lateral loading, including the load–displacement relationships, the contact stress between steel tube and concrete and the axial load distribution among inner CFST and outer RC components. Meanwhile, comparisons on the behavior of concrete-encased CFST, conventional CFST and RC columns are also conducted. Thirdly, to provide a moment versus curvature hysteretic model using the verified FEA model, which can reasonably predict the behavior of composite columns under cyclic lateral loading.

---

* Corresponding author.
  E-mail address: iliwei@tsinghua.edu.cn (W. Li).
[1] National 1000-talent Chair Professor at Tsinghua University.

Nomenclature

A	Cross-sectional area of concrete-encased CFST
A_0	Cross-sectional area of hoop-confined concrete
A_{core}	Cross-sectional area of core concrete in CFST
A_h	Cross-sectional area of stirrup
A_l	Cross-sectional area of longitudinal reinforcement
A_{out}	Cross-sectional area of outer concrete
A_s	Cross-sectional area of steel tube of CFST
B	Cross-sectional width
c	The distance from neutral axis to edge of outer compressive zone
D	Steel tube diameter of CFST
D/B	Tube diameter to cross-sectional width ratio
E_c	Modulus of elasticity of concrete
E_s	Modulus of elasticity of steel
f_c	Compressive strength of concrete
$f_{c,core}$	Compressive strength of core concrete
$f_{c,out}$	Compressive strength of outer concrete
$f_{cu,core}$	Cube strength of core concrete
$f_{cu,out}$	Cube strength of outer concrete
f_c'	Cylinder strength of concrete
f_{yh}	Yield strength of stirrup
f_{yl}	Yield strength of longitudinal reinforcement
f_{ys}	Yield strength of steel tube
h_e	Equivalent damping coefficient
l_h	Total length of stirrup in cross section
M	Moment
M_p	Ultimate moment
M_y	Yield moment
N_0	Axial load
N_u	Column compressive strength
N_{out}	Axial load of outer concrete
n	Axial load level ($n = N_0/N_u$)
P	Lateral load
R_{area}	Ratio of sectional area of column to that of the concrete-encased CFST column
R_{con}	Ratio of volume of concrete of column to that of the concrete-encased CFST column
R_s	Ratio of volume of total steel of column to that of the concrete-encased CFST column
s	Stirrup spacing
t	Thickness of steel tube in CFST
α_l	Longitudinal reinforcement ratio ($= A_l/A_{out}$)
α_s	Steel ratio of CFST ($= A_s/A_{core}$)
Δ	Lateral displacement
ϕ	Curvature
ϕ_p	Curvature corresponding to M_p
ξ	Confinement factor of CFST ($= \alpha_s f_{ys}/f_c$)
λ_s	Stirrup characteristic value ($= \rho_v f_{yh}/f_c$)
μ	Ductility coefficient
ρ_v	Volumetric ratio of stirrups ($= A_h \cdot l_h/A_0/s$)
v_s	Poisson's ratio of steel

2. FEA model and verifications

The software package of ABAQUS/Standard module [7] was employed to conduct the finite element analysis. Fig. 2 depicts the schematic view of the FEA model.

2.1. Material properties

(1) Steel.

The behavior of steel was modeled by a combination of isotropic and kinematic hardening models with a von Mises yield criterion and an associated plastic flow rule. The five-stage and bi-linear stress–strain relations provided by Han et al. [8] and Zhao et al. [9] were used to simulate uniaxial stress–strain relations of steel tube and reinforcements, respectively. Young's modulus E_s and Poisson's ratio v_s was set to be 206,000 N/mm² and 0.3, respectively.

(2) Concrete.

The concrete damaged plasticity model with a non-associated plastic flow rule and isotropic damage was used to simulate the performance of cyclically loaded concrete. The concrete cross section was divided into three parts according to different confinement as follows: the core concrete, the hoop-confined concrete and the cover concrete [1], as shown in Fig. 2(a). The stress–strain relations proposed by Han et al. [8], Han and An [1] and Attard and Setunge [10] were used to describe the uniaxial compressive stress–strain relations of the core concrete, the hoop-confined concrete and the cover concrete, respectively. The accuracy of the above model was verified by An and Han [3] under monotonic loading of combined compression and bending. As the stress–strain relation under monotonic loading is an approximation of the skeleton curve under cyclic loading, it was used herein for cyclic loading in this paper. The tensile performance of concrete was described by the tensile curve proposed by Shen et al. [11] for all kinds of concrete, which could also be found in Han et al. [8]. The elastic modulus E_c was determined as $4730\sqrt{f_c'}$ [12], and Poisson's ratio v_c was set as 0.2.

For the concrete damaged plasticity model, the tensile damage variable d_t and the compressive damage variable d_c were introduced to describe the evolution of concrete damage under tension and compression, respectively. For the definition methods for damage variables, Birtel and Mark [13] suggested the plastic strain to be the proportion of the inelastic strain. Li and Han [14] employed the assumption of "focal points", which considered that all unloading curves were pointing at virtual points in the uniaxial stress–strain plane. The comparison of analytical and experimental loading–unloading curves for concrete materials [15,16] using these two different definitions of damage variables is depicted in Fig. 3. It is shown that for the concrete under compression, the unloading stiffness using these two methods is similar. While for the concrete under tension, the predicted results using Li and Han's method are closer to the measured ones. Moreover, the convergence of the FEA model using Li and Han's method is better. The damage variable definition method proposed by Li and Han was adopted in the FEA model for further analysis, as it could predict the behavior of both unconfined concrete and concrete confined by the steel tube with a good accuracy [14], while the method presented in [13] may overestimate the damage for the tube-confined concrete. Based on extensive FEA trials, tensile and compressive stiffness recovery factors w_t and w_c were set as 0 and 0.5, respectively.

2.2. Element types, boundary conditions and steel-concrete interface

One fourth of the composite column was modeled due to the symmetry about xy and yz planes, as shown in Fig. 2(b). The concrete, steel tube and steel reinforcements were simulated by 8-node brick element (C3D8R), 4-node shell element (S4R) and 2-node truss element (T3D2), respectively. The mesh convergence study was performed to determine a proper mesh density, and the typical meshed numerical specimen is shown in Fig. 2.

A rigid block was created to model the support and tied with the column end. The displacements in x, y directions and rotations around y, z axes on the middle line of the support were constrained. Two rigid loading plates were created for lateral loading on top and bottom surfaces of the column. The boundary conditions are presented in Fig. 2(b). Two loading steps were employed for the member. A constant axial compressive load was applied at the end of member first, and then the cyclic load was applied by the displacement controlled method.
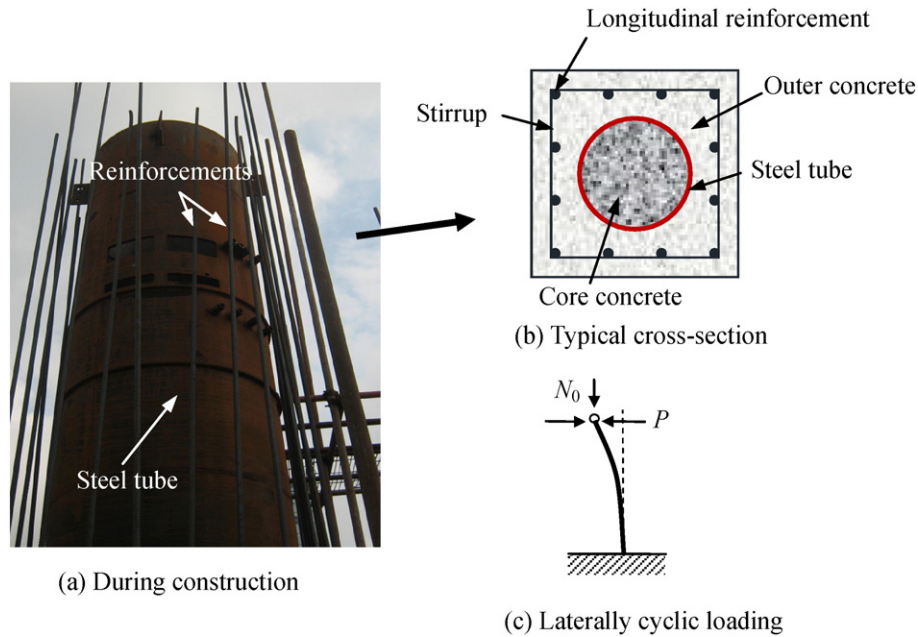
Fig. 1. Concrete-encased CFST column.

It is better to designate the hysteretic model to simulate the interface behavior in the numerical model. Applying the hysteretic model to the steel–concrete interfaces could enhance the accuracy of the calculation result. However, according to the experimental results of concrete-encased CFST columns under cyclic lateral loading [4,5,6], no sign of interface slippage was found between the steel tube and outer concrete, which implies that the interactions behave elastically during the loading. Moreover, the modeling difficulty is increased and numerical non-convergence may occur when hysteretic contact model is applied. Therefore the surface-based interaction between the steel tube and concrete was tentatively used in the cyclic simulation. In previous numerical study [14], the same surface-based interaction was applied for CFST structures under cyclic loading and was found to be adequate for the simulation. In this model, the Coulomb friction model was applied in the tangential direction and the hard-contact model was applied in the normal direction [3,14], where the frictional factor was taken as 0.6. For steel reinforcements, the integrity of the steel–concrete interface was also kept after the test. Therefore all longitudinal reinforcements and stirrups were assumed to be embedded in concrete elements. The verification shows that

the proposed contact model could also provide results with reasonable accuracy.

2.3. Verifications of the FEA model

The FEA model was verified by previous experimental results of concrete-encased CFST columns under cyclic loading. The details of the test data from literature are listed in Table 1, where B is the cross-sectional width; D and t are the diameter and thickness of the steel tube of the CFST, respectively; $f_{cu,out}$ and $f_{cu,core}$ are the cube strength of the outer and core concrete, respectively; f_{ys} and f_{yl} are the yield strength of the steel tube and longitudinal reinforcement, respectively; N_0 is the constant axial load applied before cyclic loading.

(1) Failure modes

Fig. 4(a) and (b) shows the measured and predicted failure modes of outer concrete and inner CFST for the specimen CCS10 [5] under cyclic loading, respectively. It is shown that in the experiment, the outer
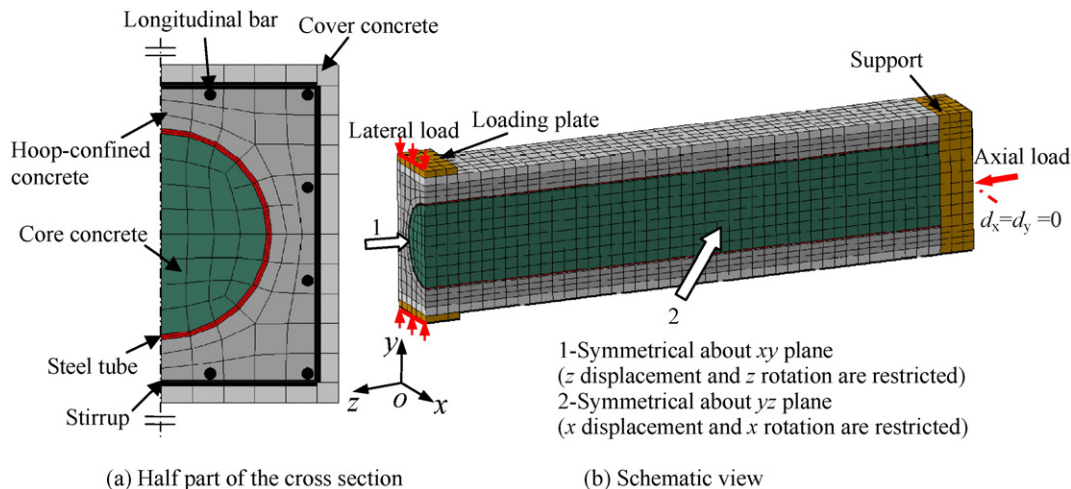

Fig. 2. A general view of FEA model.

(a) Sinha et al, 1964[15], f_c'=27.6MPa

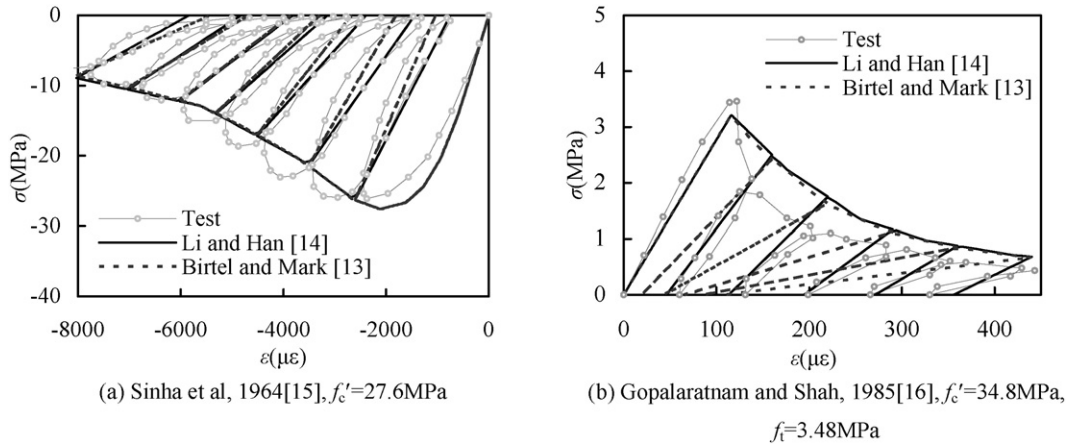(b) Gopalaratnam and Shah, 1985[16], f_c'=34.8MPa, f_t=3.48MPa

Fig. 3. Compressive and tensile loading-unloading curves for concrete.

concrete at the fixed end was crushed due to the cyclic compression and tension. Meanwhile, the interface slippage between the steel tube and outer concrete was not observed in the test. For the FEA model, the maximum principle strain vectors are near the fixed end and the outward deformation of concrete is observed at the same place. The local buckling of steel tube is observed near the fixed column end in both experimental and FEA results.

(2) Load versus displacement relations

The measured and predicted lateral load (P) versus lateral displacement (Δ) relations are compared in Fig. 5. It is found that generally good agreement is achieved between the measured and predicted results. The FEA model gives a reasonable prediction on the loading stiffness and the ultimate strength. For instance, the measured and calculated ultimate strength for CC1 is 263 kN and 269 kN, respectively, while the measured and calculated ultimate strength for S-1 is 98 kN and 92 kN, respectively. The predicted unloading stiffness is close to the measured one as well. However, the pinching phenomenon of cyclic curves observed in the experiment is more significant than that in the calculation, which may be due to the fact that the concrete damaged plasticity model could not properly simulate the crack closure of concrete from tension to compression.

(3) Ultimate strength

The measured and predicted ultimate strength is compared in Fig. 6, where the ultimate strength is the average of peak loads from both directions. More comparisons are listed in Table 1. It is found that in most cases the predicted results agree well with the experimental ones, although some specimens may not be satisfactory, which may be due to the material hardening in the experiment. The mean value and the coefficient of variation (COV) of $\overline{P}_{uc}/\overline{P}_{ue}$ are 0.930 and 0.138, respectively. In general the proposed FEA model reproduces the experimental results with reasonable accuracy.

3. Analytical behavior

The verified FEA model is used to conduct the analytical study. A typical concrete-encased CFST column is selected as follows:

- B = 400 mm; D = 250 mm; t = 5.8 mm; the steel ratio of the inner CFST, i.e. α_s ($=A_s/A_{core}$, where A_s and A_{core} are areas of the steel tube and the core concrete, respectively) is 0.1; diameters of the longitudinal reinforcement and stirrup are 14 mm and 8 mm, respectively; the spacing of the stirrups is 100 mm; the thickness of concrete cover is

Table 1
Measured and predicted ultimate strength of concrete-filled CFST columns under cyclic lateral loading.

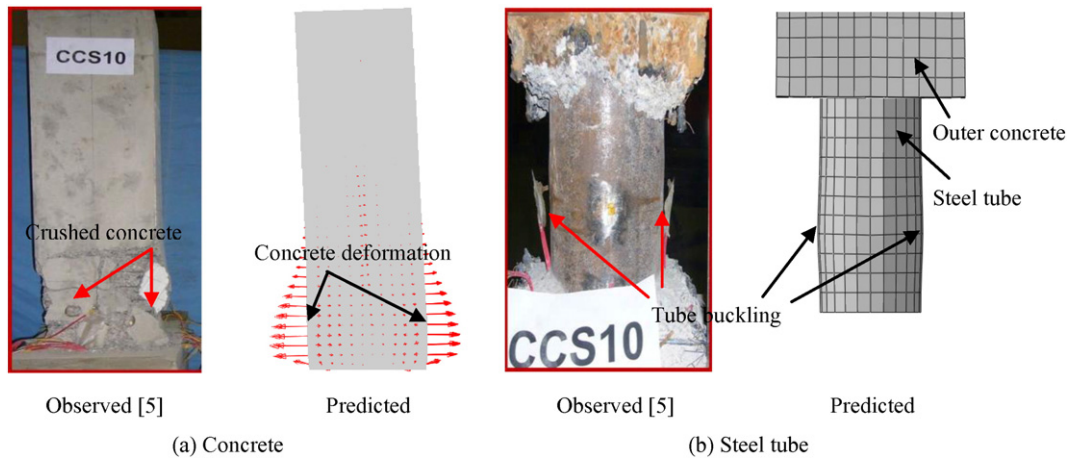| No.	Specimen label	B (mm)	$D \times t$ (mm)	$f_{cu,out}$ (N/mm²)	$f_{cu,core}$ (N/mm²)	f_{ys} (N/mm²)	f_{yl} (N/mm²)	N_0 (kN)	Measured $\overline{P}_{ue}$ (kN)	Predicted $\overline{P}_{uc}$ (kN)	$\overline{P}_{uc}/\overline{P}_{ue}$	Data sources
1	SC1	150	60×2	52.4	52.4	353	417	0	43	39	0.918	Han et al. [4]
2	SC2	150	60×2	52.4	52.4	353	417	282	56	55	0.980	
3	SC3	150	60×2	52.4	52.4	353	417	564	62	52	0.841	
4	CCS1	300	168×5.76	53.0	72.2	354	391	1038	268	267	0.994	Ji et al. [5]
5	CCS2	300	168×5.76	53.0	72.2	354	391	1025	266	244	0.916	
6	CCS3	300	168×5.76	54.0	67.3	354	391	1377	243	248	1.021	
7	CCS4	300	168×5.76	54.0	67.3	354	391	1365	234	239	1.022	
8	CCS5	300	168×5.76	58.3	68.7	354	391	1708	252	267	1.060	
9	CCS6	300	168×5.76	58.3	68.7	354	391	1697	250	251	1.004	
10	CCS7	300	168×5.76	59.4	74.1	354	391	2045	242	249	1.030	
11	CCS8	300	168×5.76	59.4	74.1	354	391	2040	261	257	0.986	
12	CCS9	300	168×5.76	57.1	73.1	354	391	2201	263	262	0.998	
13	CCS10	300	168×5.76	57.1	73.1	354	391	2188	281	283	1.010	
14	S-1	202	84.4×2.5	42.1	85.5	274	405 or 350	670	97	92	0.949	Li et al. [6]
15	S-2	200	84.4×2.5	53.8	85.5	274	405 or 350	870	146	97	0.664	
16	S-3	200	84.4×2.5	53.2	85.5	274	405 or 350	1063	166	102	0.617	
17	S-4	200	89.0×5.0	72.0	85.5	274	405 or 350	1081	169	136	0.802	
					Mean (μ)						0.930	
					COV						0.138	

Fig. 4. Comparison of failure modes between measured and predicted results under cyclic lateral loading.
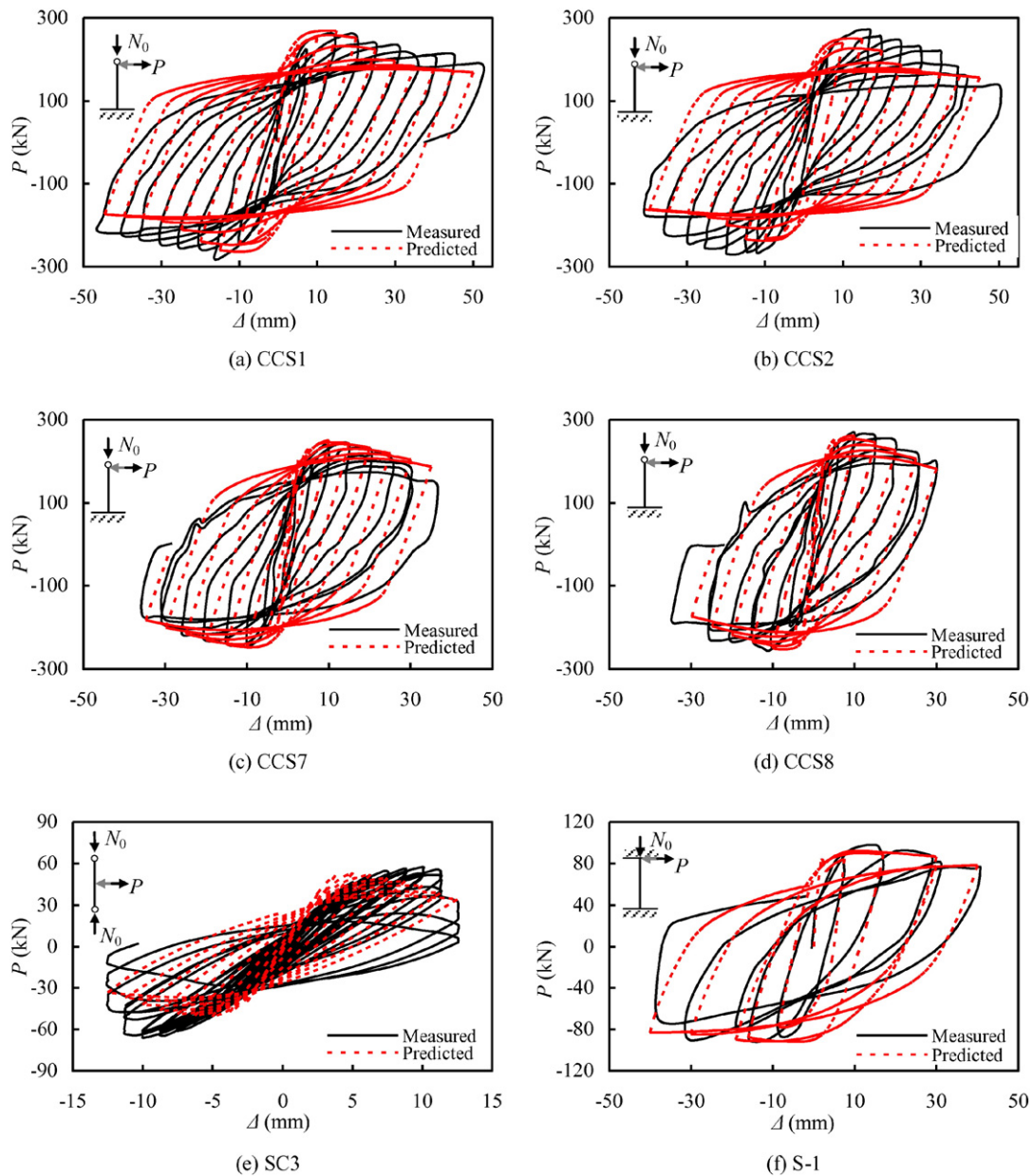

Fig. 5. Comparison of load versus displacement relations between measured and predicted results.
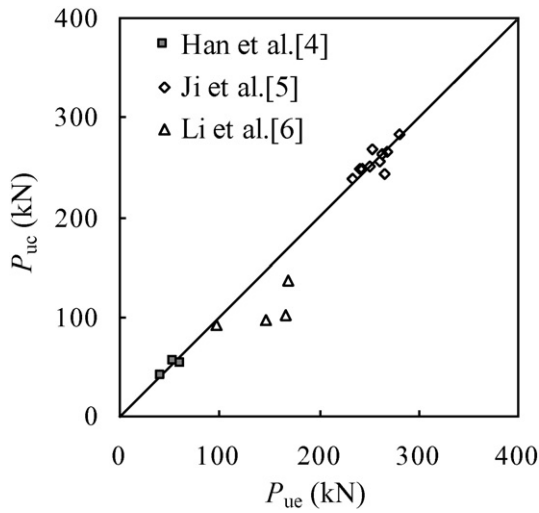
Fig. 6. Comparison of ultimate strength.

20 mm; the longitudinal reinforcement ratio α_l ($=A_l/A_{out}$, where A_l and A_{out} are areas of the longitudinal reinforcements and the outer concrete, respectively) is 1.66%; the volumetric ratio of stirrups ρ_v ($=A_h \cdot l_h/A_0/s$, where A_h is the cross-sectional area of stirrup, l_h is the total length of stirrup in cross section, A_0 is the cross-sectional area of hoop-confined concrete and s is the spacing of stirrups) is 1%; the stirrup characteristic value of outer concrete λ_s ($=\rho_v f_{yh}/f_{c,out}$, where $f_{c,out}$ is the axial compressive strength of the outer concrete according to Chinese code for design of concrete structures [17]) is 0.125.

The material properties are as follows:

- $f_{ys} = 345$ N/mm^2; $f_{yl} = 335$ N/mm^2; the yield strength of stirrup $f_{yh} = 335$ N/mm^2; $f_{cu,out} = 40$ N/mm^2 and $f_{cu,core} = 60$ N/mm^2.

The effective length l_0 between two rotation centers at the ends of column is 3300 mm. The axial load level n ($=N_0/N_u$, where N_0 is the axial load applied to the composite column; N_u is the axially compressive capacity calculated by current FEA model) is set to be 0.4. The testing program in ATC-24 [18] is adopted for the cyclic loading. Only one fourth of the specimen is modeled for the symmetry.
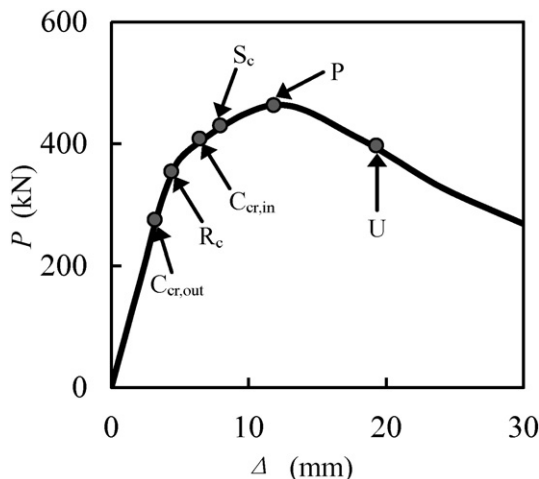

Fig. 7. Typical P-Δ envelope curve.

## 3.1. Analysis of full-range load–displacement envelope curve

Fig. 7 shows a typical P-Δ envelope curve of the concrete-encased CFST column, which is obtained by connecting peak points of every loading cycle. Six characteristic points are marked in this curve to analyze the behavior of composite column at different stages as follows: Point $C_{cr,out}$, cracking of the cover concrete; Point R_c, initial yielding of the longitudinal reinforcement under compression; Point $C_{cr,in}$, cracking of the core concrete; Point S_c, initial yielding of the steel tube under compression; Point P, the ultimate strength; Point U, the load falls to 85% of the ultimate strength.
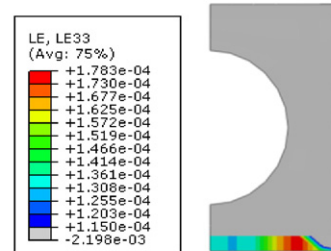
1) Point $C_{cr,out}$

The Point $C_{cr,out}$ indicates the cracking of the cover concrete. The stiffness of the P-Δ envelope curve begins to decrease slightly due to the cracks after Point $C_{cr,out}$. Fig. 8(a) shows the maximum principle stress vectors of outer concrete at Point $C_{cr,out}$, where arrows represent the directions of the maximum principle stress. Although the concrete damage plasticity model could not provide visualization of cracks, the direction of the maximum principle stress is perpendicular to that of the concrete crack. Therefore the direction and magnitude of the maximum principle stress can reflect the direction and distribution of cracks. It is shown that vertical initial cracks occur at the tensile zone at the mid-span of the column. At Point $C_{cr,out}$, the tensile longitudinal strain at the mid-span exceeds the cracking strain of concrete, as shown in Fig. 8(b), while the stress of steel reinforcements and steel tube is far less than the yield strength. The inner CFST component almost behaves elastically at Point $C_{cr,out}$.

2) Point R_c

The Point R_c indicates the initial yielding of the longitudinal reinforcement under compression. The stiffness of the P-Δ envelope curve begins to decrease obviously from Point R_c to Point P. The curve shows elasto-plastic behavior after Point R_c. As the increase of the lateral displacement, the neutral axis moves towards the compressive side due to the cracking of outer concrete. The stress of the longitudinal reinforcement under compression almost reaches the yield strength at Point R_c as shown in Fig. 9(a) while that of the longitudinal reinforcement under tension is relatively small. Fig. 9(b) gives the maximum principle stress vectors of outer concrete at Point R_c. It can be seen that the intensity of the stress increases at the tensile zone of the
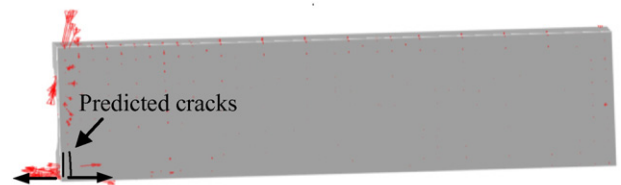
(a) Maximum principle stress vectors of outer concrete

(b) Longitudinal strain distribution of outer concrete at the mid-span

Fig. 8. Stress and strain of outer concrete at Point $C_{cr,out}$.

(a) Stress distribution (S11 in MPa) of longitudinal reinforcements

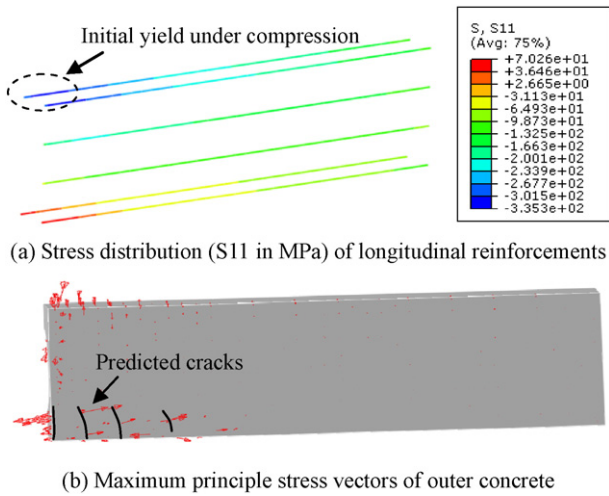(b) Maximum principle stress vectors of outer concrete

Fig. 9. Stress of longitudinal reinforcements and outer concrete at Point R_c.

outer concrete from Point $C_{cr,out}$ to Point R_c. For the inner CFST component, the stress of the steel tube is still less than the yield strength and the intensity of the maximum principle stress is very small in the core concrete at Point R_c.

3) Point $C_{cr,in}$

The Point $C_{cr,in}$ indicates cracking of the core concrete of the inner CFST component. As the neutral axis gradually moves up, the bottom zone of the core concrete is under tension at Point $C_{cr,in}$. The maximum principle stress vectors of core and outer concrete at Point $C_{cr,in}$ is given in Fig. 10(a) and (b), respectively. The maximum longitudinal strain of the core concrete at the mid-span presented in Fig. 10(c) is more than the cracking strain of concrete. The cracking area of the outer concrete expands when compared to the last point.
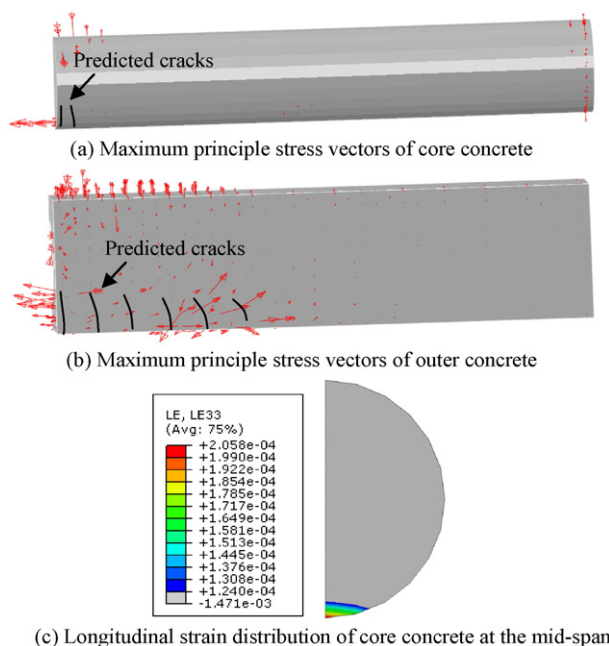
4) Point S_c

(a) Maximum principle stress vectors of core concrete

(b) Maximum principle stress vectors of outer concrete

(c) Longitudinal strain distribution of core concrete at the mid-span

Fig. 10. Stress and strain of core and outer concrete at Point $C_{cr,in}$.

The Point S_c indicates the initial yielding of the steel tube of the inner CFST component under compression. The longitudinal stress distribution of the steel tube is shown in Fig. 11. As the lateral load increases, the stress of steel tube increases continuously and reaches the yield strength at Point S_c. The tensile stress of the steel tube is less than the yield strength.

5) Point P

The Point P indicates that the ultimate strength is reached. Fig. 12(a) shows the maximum principle stress vectors of concrete at Point P. It can be found that several main cracks are formed near the mid-span. The longitudinal stress at the top of the core concrete is higher than the cylinder compressive strength ($f_{c,core,} = 51 \text{ N/mm}^2$) owing to the confinement provided by the steel tube, as shown in Fig. 12(b). The neutral axis locates between the central line of the cross section and the tensile fiber at the bottom of the core concrete. The longitudinal strains of the outer concrete on the edge of the compressive zone are larger than the crushing strain of the RC column ($\varepsilon_{cu} = 3300 \text{ με}$) according to GB50010-2010 [17], which indicates that this part of concrete is crushed. Meanwhile, stirrups yield at this point, as shown in Fig. 12(c), and the tensile stresses of the steel tube and longitudinal reinforcements are less than the tensile yield strength. The failure mode is a compression-controlled one according to An and Han [3].

6) Point U

The load decreases after Point P due to the material deterioration. The Point U corresponds to the stage when the load falls to 85% of the ultimate strength. The cracking zone expands to a farther region from the mid-span and several shear cracks occur near the column end from Point P to Point U, as shown in Fig. 13(a). The average longitudinal stress of the outer concrete is less than 10 MPa, which indicates that the outer concrete is severely damaged when the column fails. Fig. 13(b) shows that the neutral axis of the cross section moves towards the tensile side for more axial load is resisted by the inner CFST component during the loading. The whole cross section of the core concrete of the inner CFST component is under compression. Fig. 13(c) shows that the steel tube and longitudinal reinforcements under tension have yielded.

3.2. Contact stress between steel tube and concrete

The outer concrete, steel tube, core concrete and longitudinal reinforcements work together to resist the cyclic loading. It is important to understand the composite effect between these components. The normal stress develops between the outer concrete, steel tube and core concrete, which causes confinement effect to the components. The normal stress redistributes when the lateral displacement increases. When the ultimate strength is reached, the average longitudinal stress of the core concrete is still high owing to the confinement of the steel tube, and the local outward buckling of the inner steel tube does not occur owing to the support of the outer concrete.
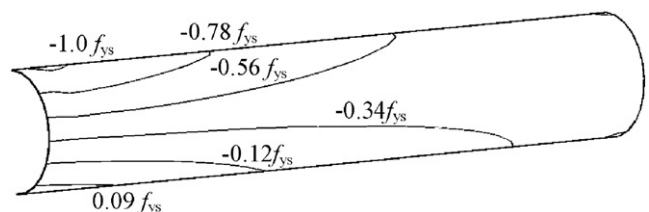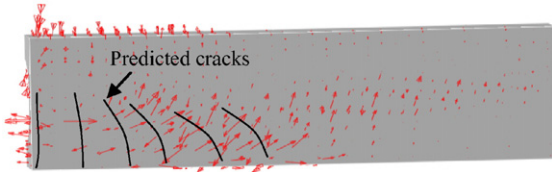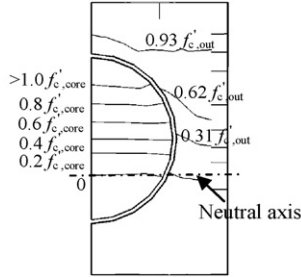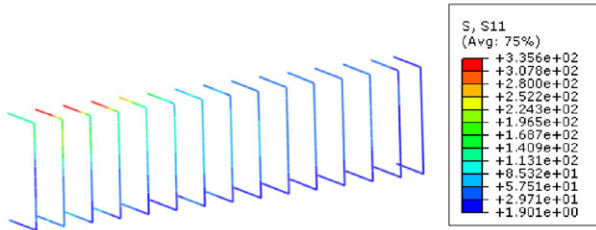

Fig. 11. Longitudinal stress distribution (S22) of steel tube at Point S_c.

(a) Maximum principle stress vectors of outer concrete

(b) Stress distribution (S33) of concrete at the mid-span

(c) Stress distribution (S11 in MPa) of stirrups

Fig. 12. Stress of concrete and stirrups at Point P.

The normal contact stress between the steel tube and core concrete, as well as that between the steel tube and outer concrete of the mid-span cross section at different displacement levels is shown in Fig. 14(a) and (b), respectively. The contact stress is parallel to the normal directions of the tube surfaces. Points 1 and 3 marked in Fig. 14 are at the tensile and compressive sides under positive loading, respectively. Before the cyclic loading is applied, i.e., $\Delta = 0$, the contact stress for Points 1, 2 and 3 is almost the same for the whole cross section is under uniform compression. The contact stress inside and outside the steel tube has a similar trend.

It can be seen in Fig. 14 that the variation trend of contact stress at Points 1 and 3 is opposite: the contact stress at Point 1 increases while that at Point 3 decreases. The reason is that the longitudinal stress of the concrete caused by lateral displacement is in opposite directions at Points 1 and 3, and higher longitudinal stress of the concrete leads to higher contact stress between steel tube and concrete. For Point 3, the contact stress increases with the increase of positive displacement level until the ultimate strength of the column is reached. It begins to descend afterwards due to the crush of the outer concrete. Meanwhile, the contact stress at negative displacement levels keeps low for the cracking of concrete. The contact stress of Point 2 is always low despite the loading direction.

3.3. Axial load distribution among components

The axial load distribution among different components could affect the design of concrete-encased CFST columns. The parametric study is conducted to analyze influences of key parameters on the axial load distribution to each component. Two parameters, the axial load level n and the ratio of diameter of steel tube to cross-sectional width D/B are chosen to analyze their influences for they affect the value of axial load resisted by different components before cyclic loading.

(1) Influence of n

The influence of the axial load level on the axial load distribution is depicted in Fig. 15(a). The values of N_{out}/N for different axial load levels before the cyclic loading are around 0.6, where N_{out} is the summation of axial loads resisted by the outer concrete and the reinforcements, N is the total axial load applied. It is due to the reason that, during the elastic stage, the load distribution is related to the proportions of the compressive stiffness of different components. The elastic stiffness of the inner CFST EA_{CFST} and the outer concrete EA_{out} can be calculated in Eqs. (1) and (2) as follows:

$$EA_{CFST} = E_{s,s} \cdot A_s + E_{c,core} \cdot A_{core} \tag{1}$$

$$EA_{out} = E_{s,l} \cdot A_l + E_{c,out} \cdot A_{out} \tag{2}$$

where $E_{s,s}$, $E_{s,l}$, $E_{c,core}$ and $E_{c,out}$ are the elastic modulus of steel tube, longitudinal reinforcement, core concrete and outer concrete, respectively; A_s, A_l, A_{core} and A_{out} are the cross-sectional areas of steel tube, longitudinal reinforcement, core concrete and outer concrete, respectively. The calculated value of $EA_{out}/(EA_{CFST} + EA_{out})$ is 0.58, which is close to N_{out}/N obtained (0.6).

The value of N_{out}/N when the column fails is less than 0.5, which indicates that more than half of the axial load is resisted by the CFST component at that moment.

As shown in Fig. 15(a), N_{out}/N increases before the ultimate strength is reached when $n = 0.2$. However, N_{out}/N decreases when $n = 0.4$ or 0.6. It might be due to the following two reasons.

i) For the specimens with higher axial load level ($n = 0.4$ or 0.6), the stress level of concrete is higher, as shown in Fig. 16, which means that the damage of external concrete is more severe under high axial load. Therefore N_{out} decreases with the increase of axial load level, and a higher n leads to a faster decrease of N_{out}/N. However, for a low axial load level ($n = 0.2$), the stress of outer concrete at the compressive zone could increase further and N_{out} increases accordingly.

ii) The neutral axis is closer to the central line of the inner CFST with a lower axial load level ($n = 0.2$), which means more area of the inner CFST is under tension. Therefore the average stress of CFST under compression is low and the summation of axial load resisted by the CFST is smaller.

N_{out}/N decreases rapidly after the ultimate strength due to the crushing of outer concrete, and the axial load is gradually transferred to the inner CFST.

(2) Influence of D/B

Three composite columns with D/B of 0.5, 0.625 and 0.75 are designed for comparison of the influence on the axial load proportion, as shown in Fig. 15(b). The other parameters of the composite columns are the same with those for the column prototype defined above. It can be seen that the average N_{out}/N is lower when the D/B is higher, but D/B ratio only has minor effect on the variation tendency of the axial load distribution on components. The reason might be that the stress levels of outer and core concrete with different D/B are close to each other under axial compression alone.

It is concluded that the axial load level has obvious influence on the variation tendency of axial load distribution among different components. The proportion of axial load resisted by the outer concrete may increase under cyclic loading with a relatively low axial load level n. Meanwhile, D/B only has a minor effect on the variation tendency of the axial load distribution.
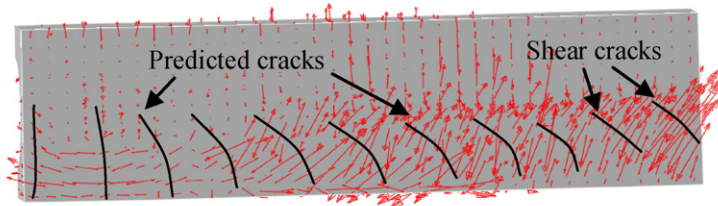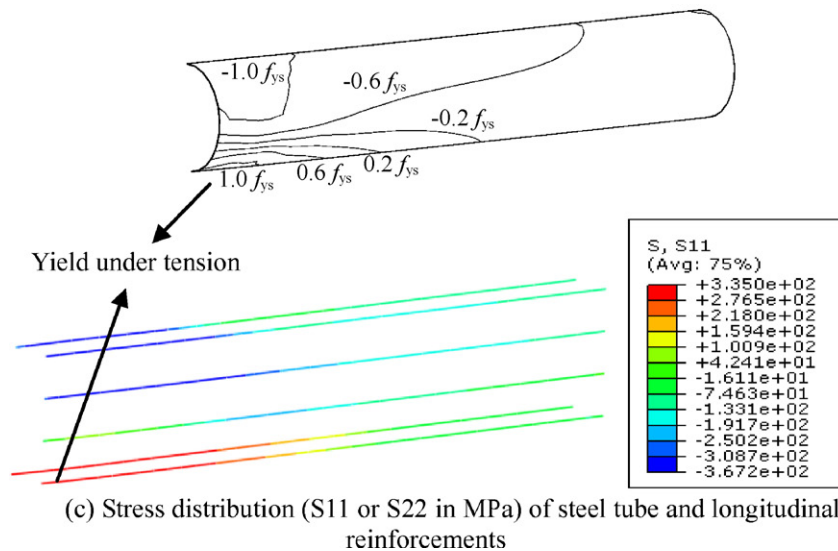
(a) Maximum principle stress vectors of concrete
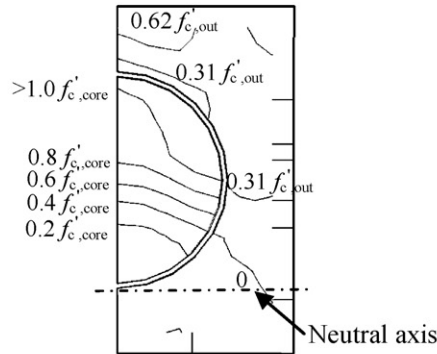
(b) Stress distribution (S33 in MPa) of concrete at the mid-span

(c) Stress distribution (S11 or S22 in MPa) of steel tube and longitudinal reinforcements

Fig. 13. Stress of concrete, steel tube and reinforcements at Point U.

3.4. Comparisons on the behavior of concrete-encased CFST, CFST and RC columns

The concrete-encased CFST column has its own characteristics when compared with conventional CFST and RC columns. Some key issues, such as the ductility and energy dissipation capacity are of key importance when designing such column members. An RC column and a circular CFST column are designed for comparison with the typical concrete-encased CFST column. These columns are designed with the following principles: the compressive capacities N_u of the columns are almost the same, and the ultimate bending moments M_p under a specific axial load level of the columns are almost the same as well. The axial load level is set to be 0.3 herein for analysis. Extensive trials through FEA model are conducted to determine the parameters of the RC column and CFST column. The parameters adopted for CFST column are: $D = 356$ mm; $t = 6.3$ mm; $f_{ys} =$ 345 N/mm²; $f_{cu,core} = 60$ N/mm². The parameters for RC column are: $B = 460$ mm; $f_{cu} = 40$ N/mm²; $f_{yl} = f_{yh} = 335$ N/mm²; diameters of longitudinal reinforcement and stirrup are 12 mm and 8 mm, respectively; the layout of the longitudinal reinforcements is the same with that in typical concrete-encased CFST column; the spacing of stirrups is 83 mm to ensure that the volumetric ratio of stirrups of the RC column is equal to that of the concrete-encased CFST column. The calculated N_u and M_p for these three columns are within a deviation of 6%.

The comparison of moment (M) versus curvature (ϕ) envelope curves is shown in Fig. 17. A curvature ductility coefficient (μ) is introduced to discuss the ductility of the columns under cyclic loading, which is defined as follows [19]:
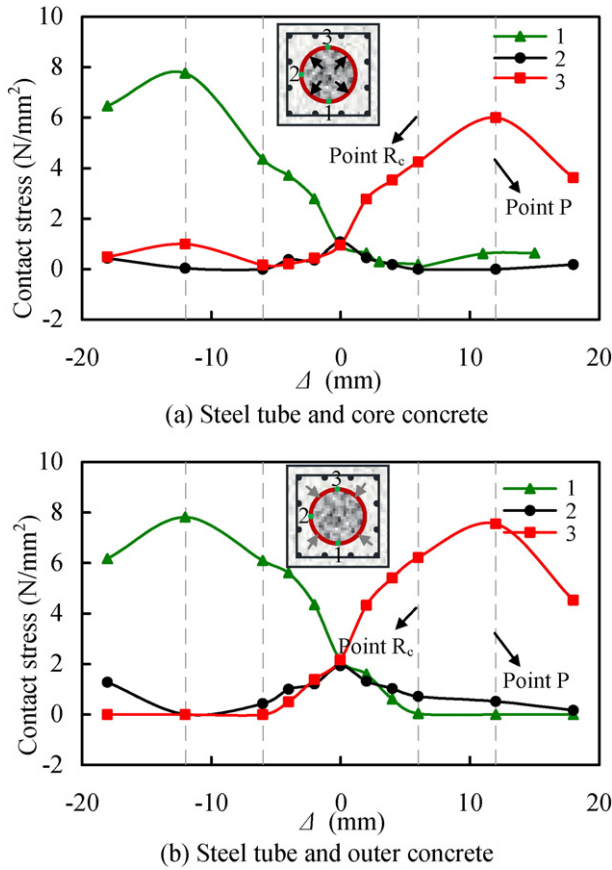
$$\mu = \frac{\phi_u}{\phi_y} \tag{3}$$

(a) Steel tube and core concrete

(b) Steel tube and outer concrete

Fig. 14. Contact stress between steel tube and concrete at the mid-span.

(a) n

(b) D/B

Fig. 15. Influence of different parameters on axial load distribution among components.

where ϕ_u and ϕ_y are the curvatures corresponding to failure and yielding on M–ϕ envelope curve.

The energy dissipation coefficient (E) and the equivalent damping coefficient (h_e) in JGJ101-96 [20] are used to assess the energy dissipation capacity of the columns. The definitions can also be found in Han and Li [21].

The calculated coefficients μ and h_e for the cycle where the ultimate strength is reached are listed in Table 2, where $\bar{\mu}$ is the averaged curvature ductility coefficient of both loading directions. The cross-sectional dimension and the material consumption are also compared in Table 2, where R_{area}, R_s and R_{con} are the ratios of cross-sectional area, the volume of total steel (steel tube, longitudinal reinforcements and stirrups) and the volume of concrete to those of the concrete-encased CFST column, respectively.

The comparison results between these specific columns are summarized as follows:

(1) Comparison between concrete-encased CFST and RC columns: the curvature ductility coefficient of the concrete-encased CFST column is about 7, which is 15% higher than that of the RC column due to the inner CFST. The concrete-encased CFST column exhibits better ductility performance under cyclic lateral loading. The consumptions of total steel and concrete for the RC column are 0.34 and 1.37 times of those for the concrete-encased CFST column, respectively. The cross-sectional area of concrete-encased CFST column is 24% less than that of RC column, which means more usable area is saved if concrete-encased CFST column is adopted.

(2) Comparison between concrete-encased CFST and CFST columns: Coefficients μ and h_e of CFST column are 31% and 54% higher than those of concrete-encased CFST, respectively. In
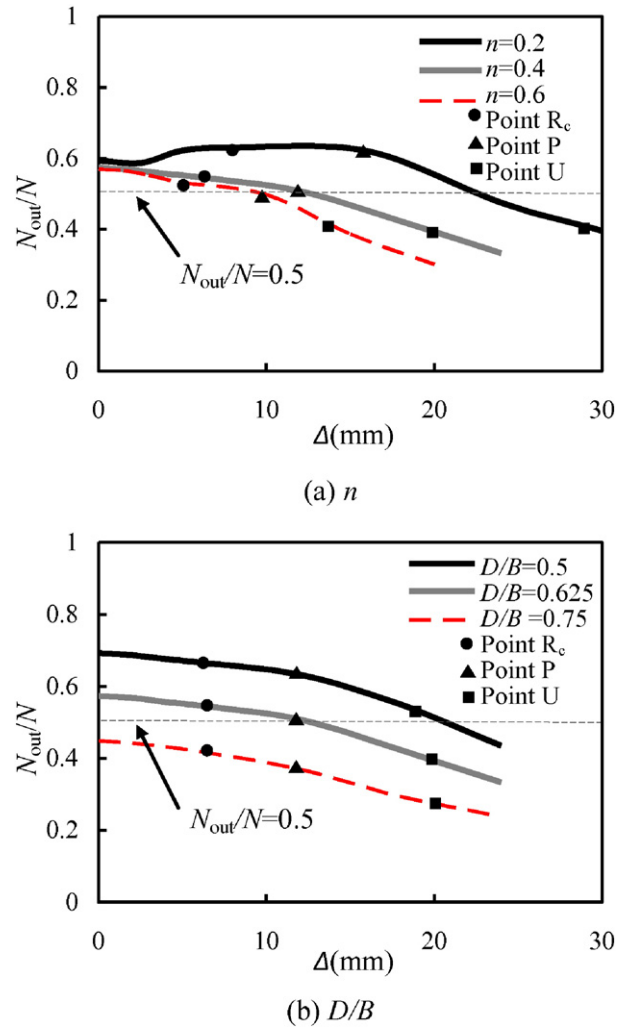
general the seismic performance of the CFST column is better. It can also be seen from Table 2 that the CFST column uses less material than the concrete-encased CFST column, and the cross-sectional profile is smaller. Nevertheless, the fire resistance of the concrete-encased CFST column is enhanced for the protection of the outer concrete, and the concrete-encased CFST column is more convenient to be connected with RC beams.

4. Parametric analysis and hysteretic model

4.1. Parametric analysis

The parameters that may affect the cyclic behavior of concrete-encased CFST column are summarized as follows:

- Material parameters: $f_{cu,core}$, $f_{cu,out}$, f_{ys}, f_{yl};
- Geometric parameters: D/B, α_s, α_l, λ;
- Loading parameters: n.

The archetype of these numerical samples is the same as that in Section 3.1. The effects of different parameters on M–ϕ envelope curves are shown in Fig. 18.

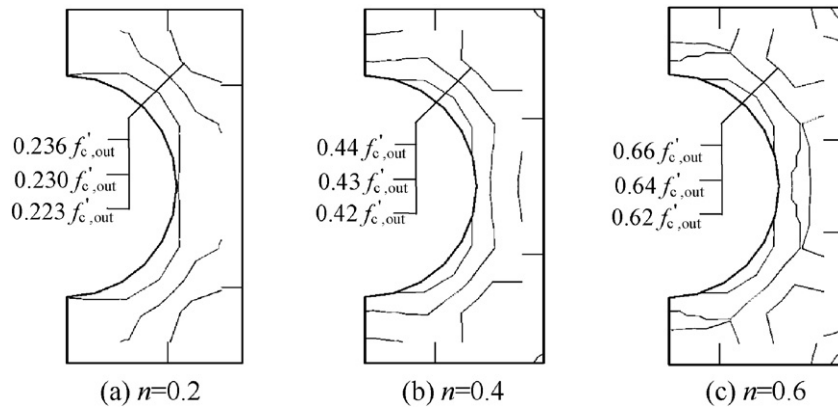(1) Effect of cube strength of core concrete $f_{cu,core}$

Fig. 16. Stress distribution (S33) of outer concrete under only axial compression.

The effect of cube strength of core concrete $f_{cu,core}$ on M–ϕ envelope curves is shown in Fig. 18(a). It can be seen that $f_{cu,core}$ has a negligible effect on the ductility. For the flexural strength, the ultimate moment M_p increases with the increase of $f_{cu,core}$.

(2) Effect of cube strength of outer concrete $f_{cu,out}$

The effect of cube strength of outer concrete $f_{cu,out}$ on M–ϕ envelope curves is shown in Fig. 18(b). It is evident that the ultimate moment and ductility are significantly influenced by $f_{cu,out}$. The ultimate moment increases by 15% when $f_{cu,out}$ varies from 30 MPa to 50 MPa. For the ductility, the sample with $f_{cu,out}$ of 30 MPa is the highest. While the ductility of the samples decreases when $f_{cu,out}$ increases, for usually the ductility is lower when the concrete strength is higher.

(3) Effect of yield strength of steel tube f_{ys}

Fig. 18(c) shows the effect of yield strength of steel tube f_{ys} on M–ϕ envelope curves. The increase of f_{ys} leads to a moderate increase in the ultimate moment and ductility.

(4) Effect of yield strength of longitudinal reinforcement f_{yl}

Fig. 18(d) shows the effect of the yield strength of longitudinal reinforcement f_{yl} on M–ϕ envelope curves. It can be found that the ultimate moment increases moderately with the increase of f_{yl}. The effect of f_{yl} is negligible on the ductility, for the longitudinal reinforcements yield under compression when the ultimate moment is reached, and the contribution to the moment is limited afterwards.

Fig. 17. Comparison of M–ϕ envelope curves.

(5) Effect of steel ratio of the inner CFST α_s

It can be seen in Fig. 18(e) that the steel ratio of the inner CFST α_s has a significant effect on both the ultimate moment and the ductility. The ultimate moment increases by 20% when α_s varies from 0.05 to 0.15. The ductility continuously increases with the increase of α_s due to the reason that a higher α_s leads to a better ductility of inner CFST component, which resists most of the load after the ultimate strength is reached.

(6) Effect of longitudinal reinforcement ratio α_l

Fig. 18(f) gives the effect of longitudinal reinforcement ratio α_l on M–ϕ envelope curves. When α_l changes from 1% to 2.32%, the ultimate moment increases by 17%. The ductility for different longitudinal reinforcement ratios is almost the same.

(7) Effect of stirrup characteristic value of outer concrete λ_s

The effect of stirrup characteristic value of outer concrete λ_s on M–ϕ envelope curves is shown in Fig. 18(g). With the increase of λ_s, the ultimate moment increases moderately. The reason is that a higher value of λ_s leads to a stronger confinement to the outer concrete and the compressive strength in uniaxial direction increases when the degree of confinement improves. Within the parameter scope in this study, λ_s seems to have a limited influence on the ductility.

(8) Effect of tube diameter to cross-sectional width ratio D/B

The effect of the tube diameter to cross-sectional width ratio D/B on M–ϕ envelope curves is shown in Fig. 18(h). The ultimate moment increases by 31% when D/B increases from 0.5 to 0.75. The D/B has negligible effect on the ductility because the effect of D/B on the crushing of the outer concrete is rather limited.
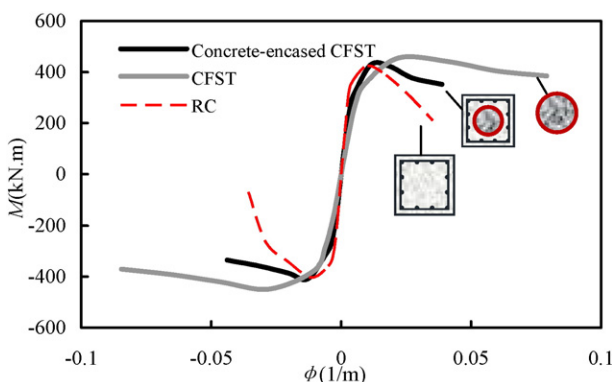
(9) Effect of axial load level n

Table 2
Comparisons between concrete-encased CFST, CFST and RC columns.

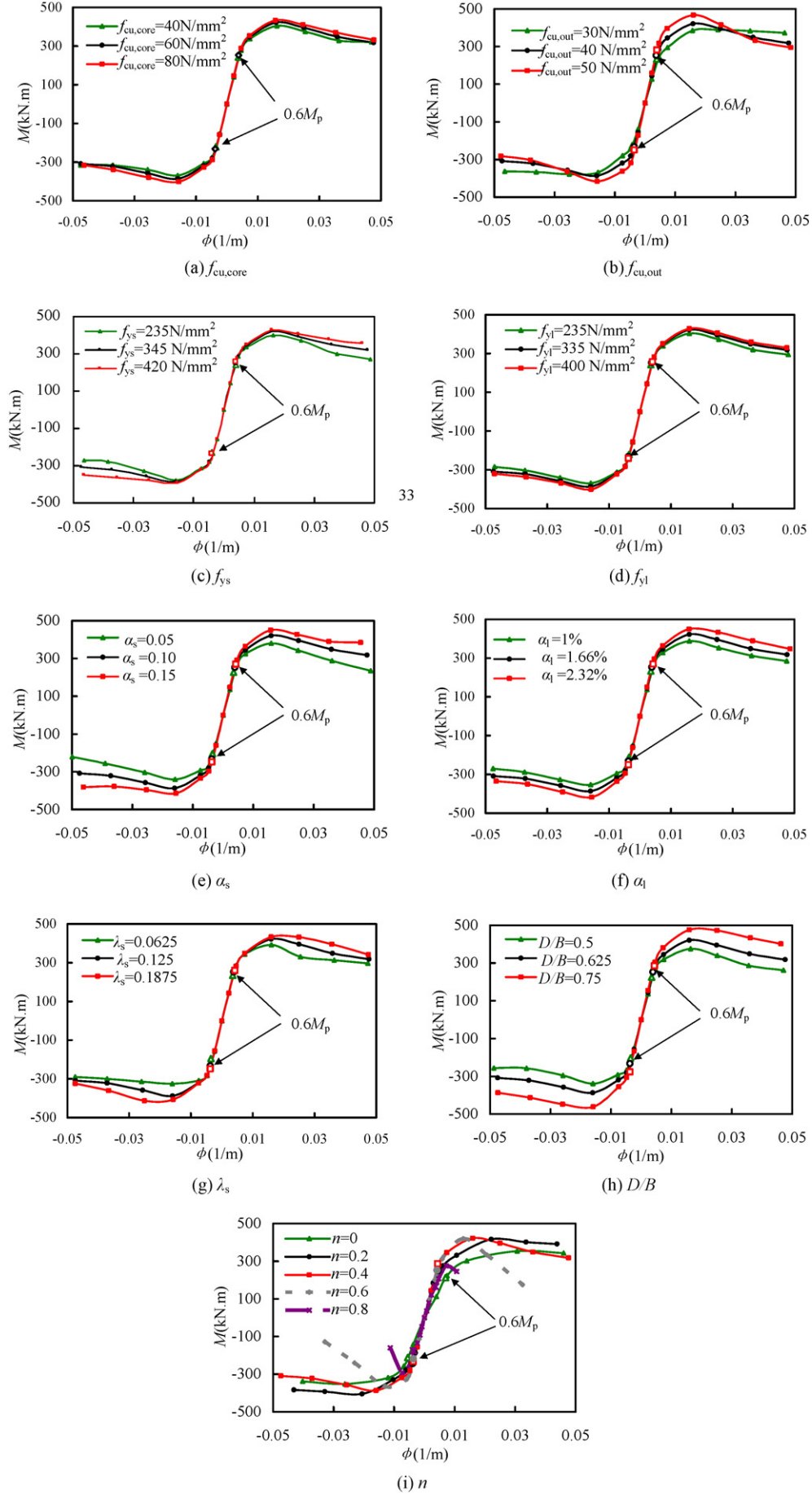| Column type	μ		$\bar{\mu}$	h_e	R_{area}	R_s	R_{con}
	(+)	(−)					
Concrete-encased CFST	6.08	7.91	6.99	0.168	1.00	1.00	1.00
CFST	9.07	9.29	9.18	0.259	0.62	0.98	0.60
RC	5.60	6.51	6.06	0.203	1.32	0.34	1.37

Fig. 18. Effect of different parameters on M-ϕ envelope curves.

The axial load level n has significant influence on M–ϕ envelope curves, as shown in Fig. 18(i). The ultimate moment increases at first and then decreases with the increase in the axial load level n, which is in accordance with the typical N_u/N_{u0}-M_u/M_{u0} interactive curve provided in An and Han [3]. The ductility decreases rapidly with the increase of axial load level, for the area of compressive zone expands with the increase of n, which leads to the decrease of ductility.

4.2. Hysteretic model

A hysteretic model for the M–ϕ relation under cyclic lateral loading is proposed for the concrete-encased CFST column. The variation ranges of parameters are: $f_{cu,core} = 40$–80 MPa; $f_{cu,out} = 30$–50 MPa; $f_{ys} = 235$–420 MPa; $f_{yl} = 235$–400 MPa; $\alpha_s = 0.05$–0.15; $\alpha_l = 1\%$–2.32%; $\lambda_s = 0.05$–0.20; $D/B = 0.5$–0.75; $n = 0$–0.8. The hysteretic model is described as follows:

4.2.1. Envelope curve

The envelope curve of the hysteretic model is modeled by a trilinear relation including the elastic stage, the elasto-plastic stage and the descending stage, as shown in Fig. 19. The parameters to be determined for the envelope curve include: the elastic stiffness K_e, the yield moment M_y, the ultimate moment M_p and the corresponding curvature ϕ_p, as well as the stiffness of descending branch K_p.

(1) Elastic stiffness (K_e)

The cross section is assumed to remain plane at the elastic stage and all components work together well. The elastic stiffness is expressed as the superposition of the contribution from all components:

$$K_e = E_{s,s} \cdot I_s + E_{s,l} \cdot I_l + E_{c,core} \cdot I_{core} + E_{c,out} \cdot I_{out} \tag{4}$$

where $E_{s,s}$, $E_{s,l}$, $E_{c,core}$ and $E_{c,out}$ are the elastic modulus of steel tube, longitudinal reinforcement, core concrete and outer concrete, respectively; I_s, I_l, I_{core} and I_{out} are the moments of inertia of steel tube, longitudinal reinforcement, core concrete and outer concrete, respectively.

(2) Yield moment (M_y) at Point A

The stiffness of the M–ϕ envelope curve begins to decrease after initial yielding of the longitudinal reinforcement under compression at Point R$_c$ (Fig. 7). The curve shows elasto-plastic behavior after Point R$_c$ therefore this point is regarded as the yield point, marked as Point A herein. Extensive numerical and experimental results show that the yield moment M_y is approximately proportional to the ultimate moment M_p, and the proportion varies from about 0.5 to 0.7. Therefore

the yield moment M_y at Point A is assumed to be proportional to M_p as follows:

$$M_y = 0.6\,M_p \tag{5}$$

where M_p is the ultimate moment defined in the following section. The coefficient is tentatively set to be 0.6 in this study. Fig. 18 also shows the points corresponding to 0.6 M_p.

(3) Ultimate moment (M_p)

It is found in experiments and numerical calculations that, for concrete-encased CFST members, the plane cross section assumption stands when the ultimate strength is reached. The equation proposed by An and Han [3] is adopted herein to predict the ultimate moment M_p of concrete-encased CFST columns under combined compression and bending

(4) Ultimate curvature (ϕ_p)

The extreme compressive strain on the edge of outer concrete is assumed to be 3300 με when the ultimate strength is reached. The corresponding ultimate curvature ϕ_p is calculated by $0.0033/c$, where c (unit in m) is the distance from the neutral axis to the edge of the compressive zone of outer concrete, and can be obtained by the method presented in An and Han [3].

(5) Descending stiffness (K_p)

For both experimental and numerical results, the descending stiffness is found to be approximately proportional to the initial loading stiffness. The parametric analysis indicates that parameters $f_{cu,out}$, α_s and n have significant influences on the stiffness of the descending branch of the M–ϕ envelope curve, as shown in Fig. 18. K_p is obtained using the regression analysis of analytical results as follows:

$$K_p = \alpha\,K_e \tag{6}$$

The coefficient $\alpha \in (-\infty, 0]$. It is found in the parametric analysis that α increases with the increase of confinement factor (ξ), which indicates that the load decrease of specimen with higher confinement factor is less significant. Meanwhile, α decreases with the increase of outer concrete strength. When the axial load level n increases, the decrease of load is more significant, which means that α also decreases. The coefficient α can be determined using the regression analysis as follows:

$$\alpha = (0.8 + 0.23\xi - 1.1C).n^2 \tag{7}$$

where $C = f_{cu,out}/30$; ξ is confinement factor of CFST calculated as $\alpha_s f_{ys}/f_{c,core}$, the axial compressive strength $f_{c,core}$ is calculated as $0.67\,f_{cu,core}$.

4.2.2. Hysteretic rules of M–ϕ relation

The stiffness degradation is observed for concrete-encased CFST columns under cyclic lateral loading. The unloading stiffness (K_r) proposed by Clough [22] is adopted herein to consider the stiffness degradation for the concrete-encased CFST column after the ultimate strength is reached:

$$K_r = \begin{cases} K_e & |\phi_r| \leq \phi_p \\ \left(\dfrac{\phi_p}{\phi_r}\right)^{\zeta} K_e & |\phi_r| > \phi_p \end{cases} \tag{8}$$

where ϕ_r is the curvature of the unloading point; ζ is an empirical coefficient and is set to be 1.2 based on numerical trials.

The schematic view of the M–ϕ relation model with hysteretic rules is presented in Fig. 19. The hysteretic rules are summarized as follows:
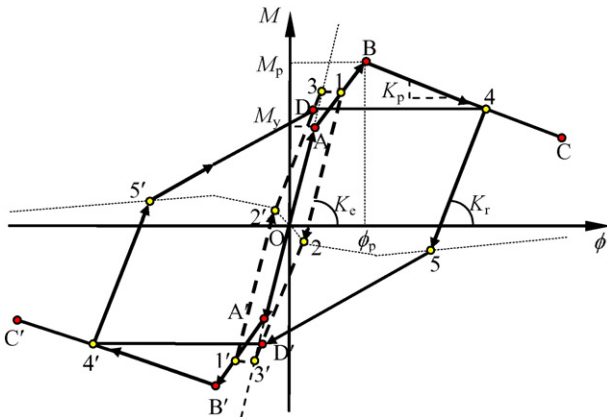

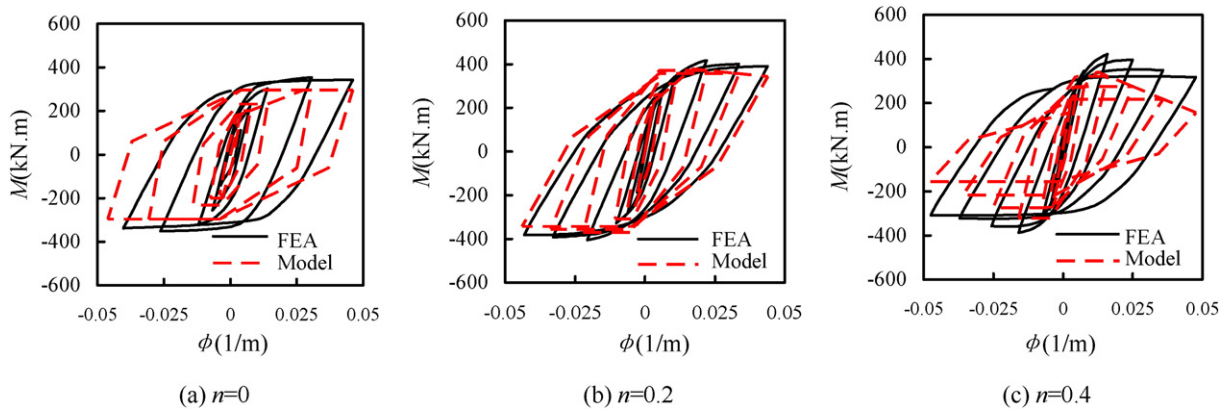Fig. 19. Hysteretic model for M-ϕ curve.

Fig. 20. Comparison between FEA and hysteretic model results.

(1) For the elastic stage, i.e., OA and OA', the model is loaded and unloaded with elastic stiffness. (2) For the elasto-plastic stage and the descending stage, the loading path is along the envelop curve, and the unloading stiffness is K_r according to Eq. (8). (3) The reloading point is on the unloading curve, while the vertical coordinate is 0.2 times of that of the unloading point. For instance, Points 2 and 5 are reloading points on the unloading curve, and the corresponding unloading points are Points 1 and 4, respectively. The vertical coordinates of Points 2 and 5 are 0.2 times of those of Points 1 and 4, respectively, while the sign is opposite. (4) The mid-target point lies on the extension line of OA or OA', and the ordinate of the mid-target point is the same as that of the final-target point. All final-target points lie on the envelop curve. For instance, Points 3' and D' are mid-target points and the corresponding final-target points are Points 1' and 4', respectively. The vertical coordinates of Points 3' and D' are the same as those of Points 1' and 4', respectively. The loading path afterward is along 3'1'2'3 or D'4'5'D.

4.2.3. Validations of hysteretic model

The comparison between results predicted from FEA model and the hysteretic model is shown in Fig. 20, where the results from FEA model are the referenced one. For the hysteretic model, M_p and ϕ_p are predicted by the method presented in Section 4.2.1. It can be seen that in general the hysteretic model could give reasonable prediction to the cyclic behavior of concrete-encased CFST members under different axial load level. However, the ultimate strength M_p in the hysteretic model is smaller than that in FEA results under high axial load levels, for the method provided in Ref. [3] is conservative in the prediction of the cross-sectional capacity.

The $M–\phi$ curves for concrete-encased CFST columns reported in literature are rather limited. Fig. 21 shows the measured and hysteretic model-predicted $M–\phi$ envelope curves of specimens SC1, SC2 and SC3 in Han et al. [4]. The details of specimens are listed in Table 1. Only the

$M–\phi$ results before reaching the ultimate strength are compared, for the measurement of the curvature is not stable after the crush of concrete in original literature. It can be seen that the ultimate moment M_p predicted is less than the measured one for the cross-sectional capacity prediction method in Ref. [3] is conservative. In general, the proposed model could give reasonable prediction on the elastic stiffness of $M–\phi$ envelope curves for specimens SC1, SC2 and SC3, although the stiffness under low axial load level maybe overestimated. More comparisons can be made when more test data is available.

5. Conclusions

The following conclusions can be drawn within the limited parameter scope of this study:

(1) A nonlinear 3-D FEA model for the concrete-encased CFST columns under cyclic lateral loading was proposed, where the damage of concrete as well as the interaction between concrete and steel were considered. It is shown that the proposed FEA model can reproduce the experimental results with good accuracy.
(2) The analytical results show that components of the composite column work together well under cyclic loading. The axial load level affects on the axial load distribution among components. The proportion of the axial load resisted by the outer reinforced concrete increases at first, and then decreases with the increase of the displacement level when under a low axial load level ($n = 0.2$).
(3) When compared with the conventional RC column having the same ultimate strength, the concrete-encased CFST column exhibits better ductility performance under cyclic loading, where the curvature ductility coefficient μ is 15% higher than the RC column. On the other hand, coefficient μ of CFST column is about 30% higher than that of concrete-encased CFST.
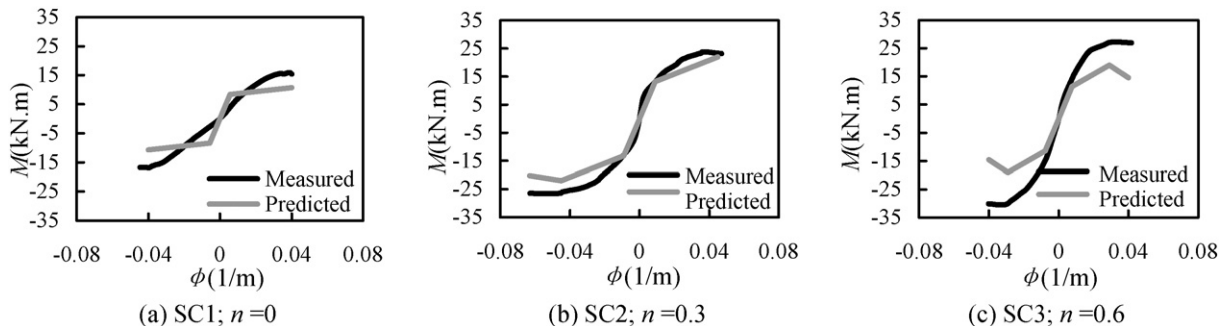

Fig. 21. Measured and predicted $M-\phi$ envelope curves.

(4) A hysteretic model of the M–ϕ relation under cyclic lateral loading was proposed for the concrete-encased CFST column, where the stiffness degradation during unloading was also taken into account. Reasonably good agreement is achieved among the hysteretic model-predicted, FEA-predicted and experimental results.

Acknowledgments

References

[1] L.H. Han, Y.F. An, Performance of concrete-encased CFST stub columns under axial compression, J. Constr. Steel Res. 93 (2014) 62–76.
[2] Y.F. An, L.H. Han, C. Roeder, Flexural performance of concrete-encased concrete-filled steel tubes, Mag. Concr. Res. 66 (5) (2014) 249–267.
[3] Y.F. An, L.H. Han, Behaviour of concrete-encased CFST columns under combined compression and bending, J. Constr. Steel Res. 101 (2014) 314–330.
[4] L.H. Han, F.Y. Liao, Z. Tao, Z. Hong, Performance of concrete filled steel tube reinforced concrete columns subjected to cyclic bending, J. Constr. Steel Res. 65 (8–9) (2009) 1607–1616.
[5] X.D. Ji, H.Z. Kang, C. Chen, J.R. Qian, Seismic behavior and strength capacity of steel tube-reinforced concrete composite columns, Earthq. Eng. Struct. Dyn. 43 (4) (2014) 487–505.
[6] H. Li, Z.Y. Wang, B. Wu, Experimental research on mechanism and seismic performance of laminated column with steel tube filled with high-strength concrete, Earthq. Eng. Eng. Vib. 19 (3) (1999) 27–33 (in Chinese).
[7] Hibbitt, Karlson & Sorensen, Inc., ABAQUS Version 6.5: Theory Manual, Users' Manual, Verification Manual and Example Problems Manual, 2005.
[8] L.H. Han, G.H. Yao, Z. Tao, Performance of concrete-filled thin-walled steel tubes under pure torsion, Thin-Walled Struct. 45 (1) (2007) 24–36.
[9] X.M. Zhao, Y.F. Wu, A.Y.T. Leung, Analysis of plastic hinge regions in reinforced concrete beams under monotonic loading, Eng. Struct. 34 (2012) 466–482.
[10] M.M. Attard, S. Setunge, Stress–strain relationship of confined and unconfined concrete, ACI Mater. J. 93 (5) (1996) 432–442.
[11] J.M. Shen, C.Z. Wang, J.J. Jiang, Finite Element Method of Reinforced Concrete and Limit Analysis of Plates and Shells, Tsinghua University Press, Beijing, 1993 (in Chinese).
[12] ACI 318-11, Building Code Requirements for Structural Concrete and Commentary, American Concrete Institute, Detroit (USA), 2011.
[13] V. Birtel, P. Mark, Parameterized Finite Element Modeling of RC Beam Shear Failure, Proceedings of the 19th Annual International ABAQUS Users' Conference, Boston, USA 23 to 25 May 2006, pp. 95–108.
[14] W. Li, L.H. Han, Seismic performance of CFST column to steel beam joint with RC slab: analysis, J. Constr. Steel Res. 67 (1) (2011) 127–139.
[15] B.P. Sinha, K.H. Gerstle, L.G. Tulin, Stress–strain relations for concrete under cyclic loading, ACI J. Proc. 61 (2) (1964) 195–211.
[16] V.S. Gopalaratnam, S.P. Shah, Softening response of plain concrete in direct tension, ACI J. Proc. 82 (3) (1985) 310–323.
[17] GB50010-2010, Code for Design of Concrete Structures, China Building Industry Press, Beijing, China, 2010 (in Chinese).
[18] ATC-24, Guidelines for Cyclic Seismic Testing of Components of Steel Structures, Applied Technology Council, California (USA), 1992.
[19] L.H. Han, Concrete-Filled Steel Tubular Structures-Theory and Practice 2nd Edition, China Science Press, Beijing, 2007 (in Chinese).
[20] JGJ 101-96, Specification of Testing Methods for Earthquake Resistant Building, China Building Industry Press, Beijing, 1997 (in Chinese).
[21] L.H. Han, W. Li, Seismic performance of CFST column to steel beam joint with RC slab: experiments, J. Constr. Steel Res. 66 (11) (2010) 1374–1386.
[22] R.W. Clough, S.B. Johnston, Effect of Stiffness Degradation on Earthquake Ductility Requirements, Proceedings of 2nd Japan Earthquake Engineering Symposium, Tokyo, Japan, 1966.